

## 9. Electromagnetic Calorimeter

### 9.1. Purpose and Design

The electromagnetic calorimeter (EMC) is designed to measure electromagnetic showers with excellent efficiency, and energy and angular resolution over the energy range from 20 MeV to 9 GeV. This capability allows the detection of photons from  $\pi^0$  and  $\eta$  decays as well as from electromagnetic and radiative processes. By identifying electrons, the EMC contributes to the flavor tagging of neutral  $B$  mesons via semi-leptonic decays, to the reconstruction of vector mesons like  $J/\psi$ , and to the study of semi-leptonic and rare decays of  $B$  and  $D$  mesons, and  $\tau$  leptons. The upper bound of the energy range is set by the need to measure QED processes, like  $e^+e^- \rightarrow e^+e^-(\gamma)$  and  $e^+e^- \rightarrow \gamma\gamma$ , for calibration and luminosity determination. The lower bound is set by the need for highly efficient reconstruction of  $B$ -meson decays containing multiple  $\pi^0$ s and  $\eta^0$ s.

#### 9.1.1. Requirements

The measurement of extremely rare decays of  $B$  mesons containing  $\pi^0$ s (*e.g.*,  $B^0 \rightarrow \pi^0\pi^0$ ) poses the most stringent requirements on energy resolution, namely of order 1–2%. Below energies of 2 GeV, the  $\pi^0$  mass resolution is dominated by the energy resolution. At higher energies, the angular resolution becomes dominant, and therefore it is required to be of the order of a few mrad.

Furthermore, the EMC has to be compatible with the 1.5 T field of the solenoid and operate reliably over the anticipated ten-year lifetime of the experiment. To achieve excellent resolution, stable operating conditions have to be maintained. Temperatures and the radiation exposure must be closely monitored, and precise calibrations of the electronics and energy response over the full dynamic range must be performed frequently.

#### 9.1.2. Design Considerations

The requirements stated above lead to the choice of a hermetic, total-absorption calorimeter, composed of a finely segmented array of thallium-doped cesium iodide (CsI(Tl)) crystals. The crystals are read out with silicon photodiodes that are matched to the spectrum of scintillation light. Recent experience at CLEO [71]

has demonstrated the suitability of this choice for physics at the  $\mathcal{T}(4S)$  resonance.

The energy resolution of a homogeneous crystal calorimeter can be described empirically in terms of a sum of two terms added in quadrature

$$\frac{\sigma_E}{E} = \frac{a}{\sqrt[4]{E(\text{GeV})}} \oplus b, \quad (6)$$

where  $E$  and  $\sigma_E$  refer to the energy of a photon and its rms error, measured in GeV. The energy dependent term  $a$  arises primarily from the fluctuations in photon statistics, but it is also impacted by electronic noise of the photon detector and electronics. Furthermore, beam-generated background will lead to large numbers of additional photons that add to the noise. This term is dominant at low energies. The constant term,  $b$ , is dominant at higher energies ( $> 1$  GeV). It arises from non-uniformity in light collection, leakage or absorption in the material between and in front of the crystals, and uncertainties in the calibrations. Most of these effects can be influenced by design choices, and they are stable with time. Others will be impacted by changes in the operating conditions, like variations in temperature, electronics gain, and noise, as well as by radiation damage caused by beam-generated radiation.

The angular resolution is determined by the transverse crystal size and the distance from the interaction point. It can also be empirically parameterized as a sum of an energy dependent and a constant term,

$$\sigma_\theta = \sigma_\phi = \frac{c}{\sqrt{E(\text{GeV})}} + d, \quad (7)$$

where the energy  $E$  is measured in GeV. The design of the EMC required a careful optimization of a wide range of choices, including the crystal material and dimensions, the choice of the photon detector and readout electronics, and the design of a calibration and monitoring system. These choices were made on the basis of extensive studies, prototyping and beam tests [72], and Monte Carlo simulation, taking into account limitations of space and the impact of other *BABAR* detector systems.

Under ideal conditions, values for the energy resolution parameters  $a$  and  $b$  close to 1–2% could

be obtained. A position resolution of a few mm will translate into an angular resolution of a few mrad; corresponding parameter values are  $c \approx 3$  mrad and  $d \approx 1$  mrad.

However in practice, such performance is very difficult to achieve in a large system with a small, but unavoidable amount of inert material and gaps, limitations of electronics, and background in multi-particle events, plus contributions from beam-generated background.

Though in CsI(Tl) the intrinsic efficiency for the detection of photons is close to 100% down to a few MeV, the minimum measurable energy in colliding beam data is expected to be about 20 MeV, a limit that is largely determined by beam- and event-related background and the amount of material in front of the calorimeter. Because of the sensitivity of the  $\pi^0$  efficiency to the minimum detectable photon energy, it is extremely important to keep the amount of material in front of the EMC to the lowest possible level.

### 9.1.3. CsI(Tl) Crystals

Thallium-doped CsI meets the needs of *BABAR* in several ways. Its properties are listed in Table 11. The high light yield and small Molière radius allow for excellent energy and angular resolution, while the short radiation length allows for shower containment at *BABAR* energies with a relatively compact design. Furthermore, the high light yield and the emission spectrum permit efficient use of silicon photodiodes which operate well in high magnetic fields. The transverse size of the crystals is chosen to be comparable to the Molière radius achieving the required angular resolution at low energies while appropriately limiting the total number of crystals (and readout channels).

## 9.2. Layout and Assembly

### 9.2.1. Overall Layout

The EMC consists of a cylindrical barrel and a conical forward endcap. It has full coverage in azimuth and extends in polar angle from  $15.8^\circ$  to  $141.8^\circ$  corresponding to a solid-angle coverage of 90% in the c.m. system (see Figure 61 and Table 12). The barrel contains 5,760 crystals arranged in 48 distinct rings with 120 identical crystals each. The endcap holds 820 crystals ar-

Table 11  
Properties of CsI(Tl) .

Parameter	Values
Radiation Length	1.85 cm
Molière Radius	3.8 cm
Density	4.53 g/cm <sup>3</sup>
Light Yield	50,000 $\gamma$ /MeV
Light Yield Temp. Coeff.	0.28%/°C
Peak Emission $\lambda_{\max}$	565 nm
Refractive Index ( $\lambda_{\max}$ )	1.80
Signal Decay Time	680 ns (64%) 3.34 $\mu$ s (36%)

ranged in eight rings, adding up to a total of 6,580 crystals. The crystals have a tapered trapezoidal cross section. The length of the crystals increases from 29.6 cm in the backward to 32.4 cm in the forward direction to limit the effects of shower leakage from increasingly higher energy particles.

Table 12

Layout of the EMC, composed of 56 axially symmetric rings, each consisting of CsI crystals of identical dimensions.

$\theta$ Interval (radians)	Length ( $X_0$ )	# Rings	Crystals /Ring
Barrel			
2.456 – 1.214	16.0	27	120
1.213 – 0.902	16.5	7	120
0.901 – 0.655	17.0	7	120
0.654 – 0.473	17.5	7	120
Endcap			
0.469 – 0.398	17.5	3	120
0.397 – 0.327	17.5	3	100
0.326 – 0.301	17.5	1	80
0.300 – 0.277	16.5	1	80

To minimize the probability of pre-showering, the crystals are supported at the outer radius, with only a thin gas seal at the front. The barrel and outer five rings of the endcap have less than  $0.3-0.6X_0$  of material in front of the crystal faces.



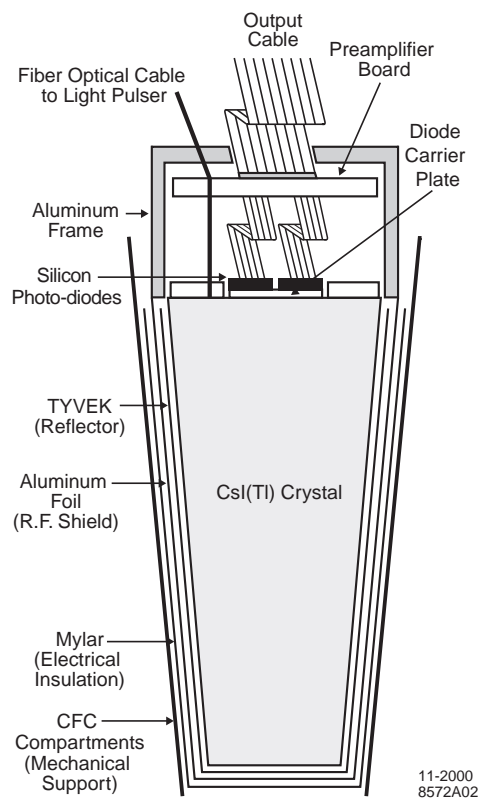


Figure 62. A schematic of the wrapped CsI(Tl) crystal and the front-end readout package mounted on the rear face. Also indicated is the tapered, trapezoidal CFC compartment, which is open at the front. This drawing is not to scale.

reflective paint [79]. The plate has two 3 mm-diameter penetrations for the fibers of the light pulser monitoring system.

As part of the quality control process, the 1.836 MeV photon line from a  $^{88}\text{Y}$  radioactive source was used to measure the light yield of every crystal-diode assembly, employing a preamplifier with  $2\ \mu\text{s}$  Gaussian shaping. The resulting signal distribution had a mean and rms width of 7300 and 890 photoelectrons/MeV, respectively; none of the crystals had a signal of less than 4600 photoelectrons/MeV [78,80].

Each of the diodes is directly connected to a low-noise preamplifier. The entire assembly is enclosed by an aluminum fixture as shown in Fig-

ure 62. This fixture is electrically coupled to the aluminum foil wrapped around the crystal and thermally coupled to the support frame to dissipate the heat load from the preamplifiers.

Extensive aging tests were performed to ascertain that the diodes and the preamplifiers met the ten-year lifetime requirements. In addition, daily thermal cycles of  $\pm 5^\circ\text{C}$  were run for many months to assure that the diode-crystal epoxy joint could sustain modest temperature variations.

#### 9.2.4. Crystal Support Structure

The crystals are inserted into modules that are supported individually from an external support structure. This structure is built in three sections, a cylinder for the barrel and two semi-circular structures for the forward endcap. The barrel support cylinder carries the load of the barrel modules plus the forward endcap to the magnet iron through four flexible supports. These supports decouple and dampen any acceleration induced by movements of the magnet iron during a potential earthquake.

The modules are built from tapered, trapezoidal compartments made from carbon-fiber-epoxy composite (CFC) with  $300\ \mu\text{m}$ -thick walls (Figure 63). Each compartment loosely holds a single wrapped and instrumented crystal and thus assures that the forces on the crystal surfaces never exceed its own weight. Each module is surrounded by an additional layer of  $300\ \mu\text{m}$  CFC to provide additional strength. The modules are bonded to an aluminum strong-back that is mounted on the external support. This scheme minimizes inter-crystal materials while exerting minimal force on the crystal surfaces; this prevents deformations and surface degradation that could compromise performance. By supporting the modules at the back, the material in front of the crystals is kept to a minimum.

The barrel section is divided into 280 separate modules, each holding 21 crystals ( $7 \times 3$  in  $\theta \times \phi$ ). After the insertion of the crystals, the aluminum readout frames, which also stiffen the module, are attached with thermally-conducting epoxy to each of the CFC compartments. The entire 100 kg-module is then bolted and again thermally epoxied to an aluminum strong-back. The

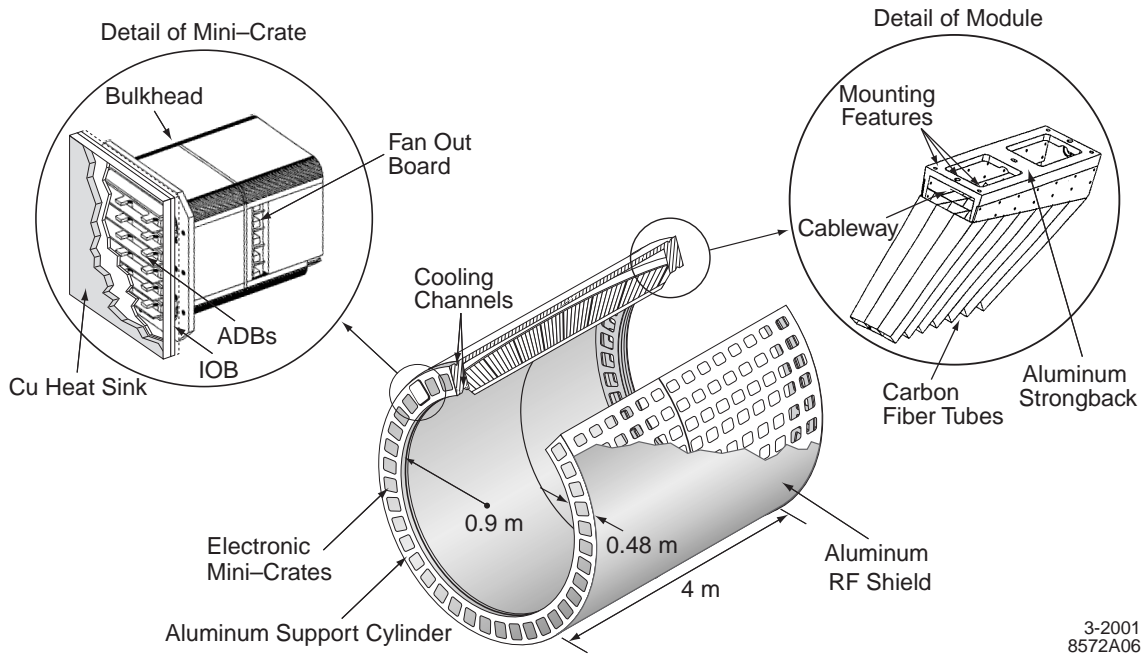


Figure 63. The EMC barrel support structure, with details on the modules and electronics crates (not to scale).

strong-back contains alignment features as well as channels that couple into the cooling system. Each module was installed into the 2.5 cm-thick, 4 m-long aluminum support cylinder, and subsequently aligned. On each of the thick annular end-flanges this cylinder contains access ports for digitizing electronics crates with associated cooling channels, as well as mounting features and alignment dowels for the forward endcap.

The endcap is constructed from 20 identical CFC modules (each with 41 crystals), individually aligned and bolted to one of two semi-circular support structures. The endcap is split vertically into two halves to facilitate access to the central detector components.

The entire calorimeter is surrounded by a double Faraday shield composed of two 1 mm-thick aluminum sheets so that the diodes and preamplifiers are further shielded from external noise. This cage also serves as the environmental barrier, allowing the slightly hygroscopic crystals to reside in a dry, temperature controlled nitrogen

atmosphere.

### 9.2.5. Cooling System

The EMC is maintained at constant, accurately monitored temperature. Of particular concern are the stability of the photodiode leakage current which rises exponentially with temperature, and the large number of diode-crystal epoxy joints that could experience stress due to differential thermal expansion. In addition, the light yield of CsI(Tl) is weakly temperature dependent.

The primary heat sources internal to the calorimeter are the preamplifiers ( $2 \times 50$  mW/crystal) and the digitizing electronics (3 kW per end-flange). In the barrel, the preamplifier heat is removed by conduction to the module strong backs which are directly cooled by Fluorinert (polychlorotrifluoro-ethylene) [81]. The digitizing electronics are housed in 80 mini-crates, each in contact with the end-flanges of the cylindrical support structure. These crates are indirectly cooled by chilled water pumped

through channels milled into the end-flanges close to the inner and outer radii. A separate Fluorinert system in the endcap cools both the 20 mini-crates of digitizing electronics and the preamplifiers.

### 9.3. Electronics

The EMC electronics system, shown schematically in Figure 64, is required to have negligible impact on the energy resolution of electromagnetic showers from 20 MeV to 9 GeV, while accommodating the use of a 6.13 MeV radioactive source for calibration. These requirements set a limit of less than 250 keV equivalent noise energy (ENE) per crystal and define an 18-bit effective dynamic range of the digitization scheme. For source calibrations, the least significant bit is set to 50 keV, while for colliding beam data it is set to 200 keV. To reach the required energy resolution at high energies, the coherent component has to be significantly smaller than the incoherent noise component. In addition, the impact of high rates of low energy (<5 MeV) beam-induced photon background needs to be minimized.

#### 9.3.1. Photodiode Readout and Preamplifiers

The ENE is minimized by maximizing the light yield and collection, employing a highly efficient photon detector, and a low-noise electronic readout. The PIN silicon photodiodes [82] have a quantum efficiency of 85% for the CsI(Tl) scintillation light [83]. At a depletion voltage of 70 V, their typical dark currents were measured to be 4 nA for an average capacitance of 85 pF; the diodes are operated at a voltage of 50 V. The input capacitance to the preamplifier is minimized by connecting the diodes to the preamplifier with a very short cable. The preamplifier is a low-noise charge-sensitive amplifier implemented as a custom application specific integrated circuit (ASIC) [84]. It shapes the signal and acts as a band-pass filter to remove high- and low-frequency noise components. The optimum shaping time for the CsI(Tl)-photodiode readout is 2–3  $\mu$ s, but a shorter time was chosen to reduce the probability of overlap with low-energy photons from beam background. The commensurate

degradation in noise performance is recovered by implementing a realtime digital signal-processing algorithm following digitization.

To achieve the required operational reliability [85] for the inaccessible front-end readout components, two photodiodes were installed, each connected to a preamplifier. In addition, all components were carefully selected and subjected to rigorous tests, including a 72-hour burn-in of the preamplifiers at 70°C to avoid infant mortality. The dual signals are combined in the postamplification/digitization circuits, installed in mini-crates at the end-flanges, a location that is accessible for maintenance.

#### 9.3.2. Postamplification, Digitization and Readout

The two preamplifiers on each crystal, A and B, each provide amplification factors of 1 and 32 and thus reduce the dynamic range of the signal that is transmitted to the mini-crates to 13-bits. A custom auto-range encoding (CARE) circuit [84] further amplifies the signal to arrive at a total gain of 256, 32, 4 or 1 for four energy ranges, 0–50 MeV, 50–400 MeV, 0.4–3.2 GeV, and 3.2–13.0 GeV, respectively. The appropriate range is identified by a comparator and the signal is digitized by a 10-bit, 3.7 MHz ADC. Data from 24 crystals are multiplexed onto a fiber-optic driver and sent serially at a rate of 1.5 Gbytes/s across a 30 m-long optical fiber to the ROM. In the ROM, the continuous data stream is entered into a digital pipeline. A correction for pedestal and gain is applied to each sample. The pipeline is then tapped to extract the input to the calorimeter trigger.

Upon receipt of the L1 *Accept* signal, data samples within a time window of  $\pm 1 \mu$ s are selected for the feature extraction. Up to now, the calorimeter feature extraction algorithm performs a parabolic fit to the peak of the signal waveform to derive its energy and time. In the future, it is planned to employ a digital filter prior to the signal fit to further reduce noise. For this filter algorithm, the frequency decomposition of an average signal pulse and the typical noise spectrum are measured for all channels and subsequently used to derive an optimum set of weights that maxi-

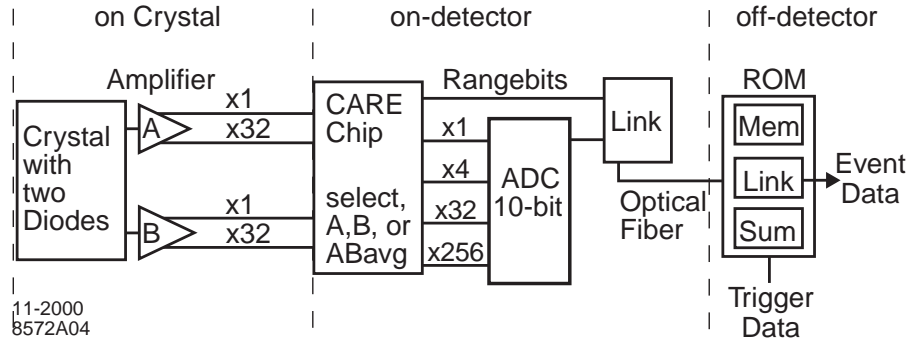


Figure 64. Schematic diagram of the EMC readout electronics.

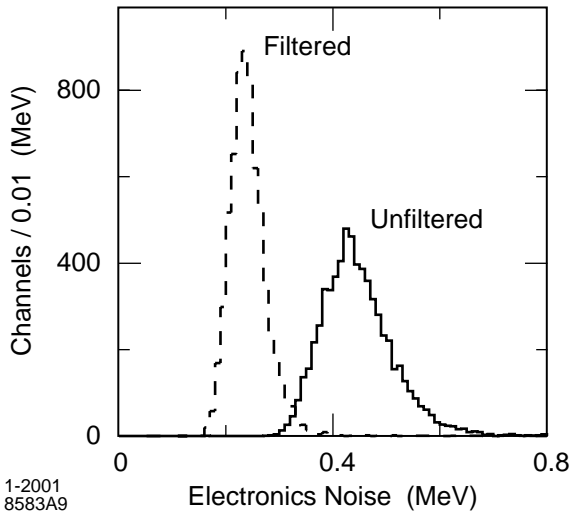


Figure 65. The distribution of equivalent noise energy (ENE) or all channels of the EMC with and without digital filtering. The data were recorded in the absence of beams by a random trigger.

mizes the signal-to-noise ratio. These weights are then applied to individual samples to obtain a filtered waveform.

The magnitude of the electronic noise is measured as the rms width of the pedestal distribution as shown in Figure 65. The observed distribution for all channels translates to an ENE

of 230 keV and 440 keV with and without digital filtering; this result is comparable to design expectations. Measurements of the auto-correlation function indicate that the coherent noise component is negligible compared to the incoherent noise, except for regions where the preamplifiers saturate (see below).

During data-taking, the data acquisition imposes a single-crystal readout threshold in order to keep the data volume at an acceptable level. This energy threshold is currently set to 1 MeV and during stable colliding beam conditions on average 1,000 crystals are read out (measured with 600 mA of  $e^-$  and 1100 mA of  $e^+$  and a random clock trigger), corresponding to an average occupancy of 16%. The electronic noise accounts for about 10%, while the remaining signals originate from beam-generated background (see Section 3). A typical hadronic event contributes signals in 150 crystals.

### 9.3.3. Electronics Calibration and Linearity

To measure pedestal offsets, determine the overall gain, and to remove non-linearities the FEE are calibrated by precision charge injection into the preamplifier input. Initially, residual non-linearities of up to 12% in limited regions near each of the range changes were observed and corrected for offline [86]. These non-linearities were traced to oscillations on the ADC cards that have since been corrected. The correction resulted in markedly improved energy resolution

at high energies. Residual non-linearities (typically 2–4%) arise primarily from cross-talk, impacting both the electronics calibrations and the colliding-beam data. The effect is largest at about 630 MeV (950 MeV) in a high (low) gain preamplifier channel, inducing a 2 MeV (6 MeV) cross-talk signal in an adjacent channel. The implementation of an energy dependent correction is expected to significantly reduce this small, remaining effect, and lead to a further improvement of the energy resolution.

#### 9.3.4. Electronics Reliability

With the exception of minor cable damage during installation (leaving two channels inoperative), the system of 13,160 readout channels has met its reliability requirements. After the replacement of a batch of failing optical-fiber drivers, the reliability of the digitizing electronics improved substantially, averaging channel losses of less than 0.1%.

#### 9.4. Energy Calibration

The energy calibration of the EMC proceeds in two steps. First, the measured pulse height in each crystal has to be translated to the actual energy deposited. Second, the energy deposited in a shower spreading over several adjacent crystals has to be related to the energy of the incident photon or electron by correcting for energy loss mostly due to leakage at the front and the rear, and absorption in the material between and in front of the crystals, as well as shower energy not associated with the cluster.

The offline pattern recognition algorithm that groups adjacent crystals into clusters is described in detail in Section 9.6.

##### 9.4.1. Individual Crystal Calibration

In spite of the careful selection and tuning of the individual crystals, their light yield varies significantly and is generally non-uniform. It also changes with time under the impact of beam-generated radiation. The absorbed dose is largest at the front of the crystal and results in increased attenuation of the transmitted scintillation light. The light yield must therefore be calibrated at different energies, corresponding to different average shower penetration, to track the effects of

the radiation damage.

The calibration of the deposited energies is performed at two energies at opposite ends of the dynamic range, and these two measurements are combined by a logarithmic interpolation. A 6.13 MeV radioactive photon source [87] provides an absolute calibration at low energy, while at higher energies (3–9 GeV) the relation between polar angle and energy of  $e^\pm$  from Bhabha events is exploited [88].

A flux of low-energy neutrons ( $4 \times 10^8/s$ ) is used to irradiate Fluorinert [81] to produce photons of 6.13 MeV via the reaction  $^{19}\text{F} + n \rightarrow ^{16}\text{N} + \alpha$ ,  $^{16}\text{N} \rightarrow ^{16}\text{O}^* + \beta$ ,  $^{16}\text{O}^* \rightarrow ^{16}\text{O} + \gamma$ . The activated  $^{16}\text{N}$  has a half-life of 7 seconds and thus does not cause radiation damage or long-term activation. The fluid is pumped at a rate of 125  $\ell/s$  from the neutron generator to a manifold of thin-walled (0.5 mm) aluminum pipes that are mounted immediately in front of the crystals. At this location, the typical rate of photons is 40 Hz/crystal.

Figure 66 shows a typical source spectrum that was derived from the raw data by employing a digital filter algorithm. For a 30-minute exposure, a statistical error of 0.35% is obtained, compared to a systematic uncertainty of less than 0.1%. This calibration is performed weekly.

At high energies, single crystal calibration is performed with a pure sample of Bhabha events [88]. As a function of the polar angle of the  $e^\pm$ , the deposited cluster energy is constrained to equal the prediction of a GEANT-based Monte Carlo simulation [89]. For a large number of energy clusters, a set of simultaneous linear equations relates the measured to the expected energy and thus permits the determination of a gain constant for each crystal. In a 12-hour run at a luminosity of  $3 \times 10^{33} \text{ cm}^{-2}\text{s}^{-1}$  some 200  $e^\pm$  per crystal can be accumulated, leading to a statistical error of 0.35%. This calibration has been performed about once per month, and will be fully automated in the future.

##### 9.4.2. Cluster Energy Correction

The correction for energy loss due to shower leakage and absorption is performed as a function of cluster energy and polar angle. At low energy ( $E < 0.8 \text{ GeV}$ ), it is derived from  $\pi^0$  decays [90].

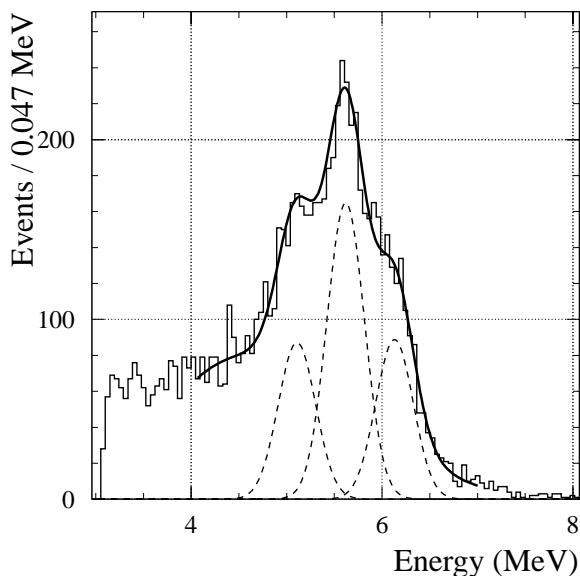


Figure 66. A typical pulse-height spectrum recorded with the radioactive source to calibrate the single-crystal energy scale of the EMC. The spectrum shows the primary 6.13 MeV peak and two associated escape peaks at 5.62 MeV and 5.11 MeV. The solid line represents a fit to the total spectrum, the dotted lines indicate the contributions from the three individual photon spectra.

The true energy of the photon is expressed as a product of the measured deposited energy and a correction function which depends on  $\ln E$  and  $\cos \theta$ . The algorithm constrains the two-photon mass to the nominal  $\pi^0$  mass and iteratively finds the coefficients of the correction function. The typical corrections are of order  $6 \pm 1\%$ . The uncertainty in the correction is due to systematic uncertainties in the background estimation and the fitting technique.

At higher energy ( $0.8 < E < 9$  GeV) the correction is estimated from single-photon Monte Carlo simulations. A second technique using radiative Bhabha events [91] is being developed. The beam energy and the precise track momenta of the  $e^+$  and  $e^-$ , together with the direction of the radiative photon, are used to fit the photon energy. This fitted value is compared to the measured

photon energy to extract correction coefficients, again as a function of  $\ln E$  and  $\cos \theta$ .

## 9.5. Monitoring

### 9.5.1. Environmental Monitoring

The temperature is monitored by 256 thermal sensors that are distributed over the calorimeter, and has been maintained at  $20 \pm 0.5^\circ\text{C}$ . Dry nitrogen is circulated throughout the detector to stabilize the relative humidity at  $1 \pm 0.5\%$ .

### 9.5.2. Light-Pulsar System

The light response of the individual crystals is measured daily using a light-pulsar system [92, 93]. Spectrally filtered light from a xenon flash lamp is transmitted through optical fibers to the rear of each crystal. The light pulse is similar in spectrum, rise-time and shape to the scintillation light in the CsI(Tl) crystals. The pulses are varied in intensity by neutral-density filters, allowing a precise measurement of the linearity of light collection, conversion to charge, amplification, and digitization. The intensity is monitored pulse-to-pulse by comparison to a reference system with two radioactive sources,  $^{241}\text{Am}$  and  $^{148}\text{Gd}$ , that are attached to a small CsI(Tl) crystal that is read out by both a photodiode and a photomultiplier tube. The system is stable to 0.15% over a period of one week and has proven to be very valuable in diagnosing problems. For example, the ability to accurately vary the light intensity led to the detection of non-linear response in the electronics [92].

### 9.5.3. Radiation Monitoring and Damage

The radiation exposure is monitored by 56 and 60 realtime integrating dosimeters (Rad-FETs) [18] placed in front of the barrel and endcap crystals. In Figure 67, the accumulated dose is compared to the observed loss in scintillation light, separately for the endcap, the forward, and the backward barrel. The dose appears to follow the integrated luminosity, approximately linearly. The light loss is greatest in the forward region corresponding to the area of highest integrated radiation dose. The size of the observed light loss is close to expectations, based on extensive irradiation tests.

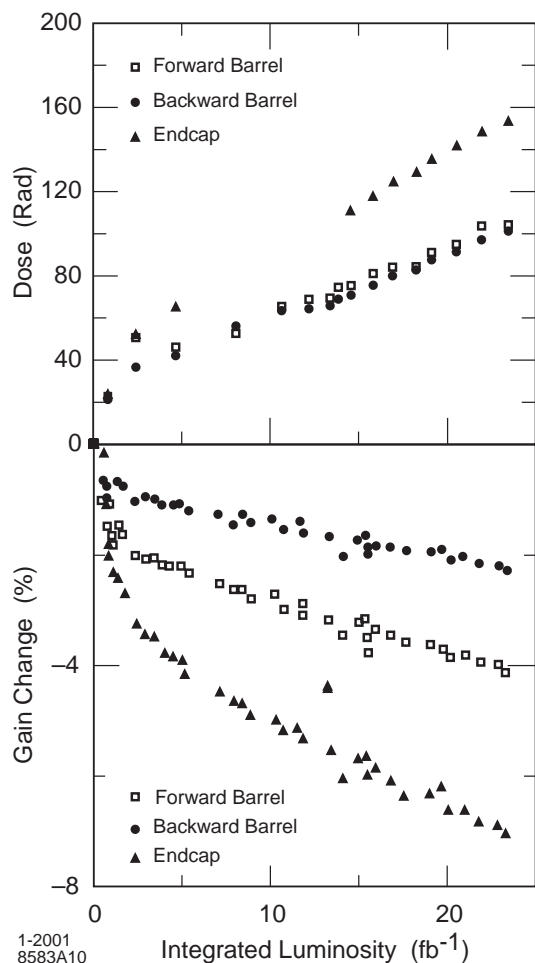


Figure 67. Impact of beam-generated radiation on the CsI(Tl) crystals: a) the integrated dose measured with RadFETs placed in front of the crystals, b) the degradation in light yield measured with the radioactive-source calibration system.

### 9.6. Reconstruction Algorithms

A typical electromagnetic shower spreads over many adjacent crystals, forming a *cluster* of energy deposits. Pattern recognition algorithms have been developed to efficiently identify these clusters and to differentiate single clusters with one energy maximum from merged clusters with more than one local energy maximum, referred to as a *bumps*. Furthermore, the algorithms deter-

mine whether a bump is generated by a charged or a neutral particle.

Clusters are required to contain at least one seed crystal with an energy above 10 MeV. Surrounding crystals are considered as part of the cluster if their energy exceeds a threshold of 1 MeV, or if they are contiguous neighbors (including corners) of a crystal with at least 3 MeV. The value of the single crystal threshold is set by the data acquisition system in order to keep the data volume at an acceptable level, given the current level of electronics noise and beam-generated background. It is highly desirable to reduce this threshold since fluctuations in the effective energy loss at the edges of a shower cause a degradation in resolution, particularly at low energies.

Local energy maxima are identified within a cluster by requiring that the candidate crystal have an energy,  $E_{LocalMax}$ , which exceeds the energy of each of its neighbors, and satisfy the following condition:  $0.5(N - 2.5) > E_{NMax}/E_{LocalMax}$ , where  $E_{NMax}$  is the highest energy of any of the neighboring  $N$  crystals with an energy above 2 MeV.

Clusters are divided into as many bumps as there are local maxima. An iterative algorithm is used to determine the energy of the bumps. Each crystal is given a weight,  $w_i$ , and the bump energy is defined as  $E_{bump} = \sum_i w_i E_i$ , where the sum runs over all crystals in the cluster. For a cluster with a single bump, the result is  $w_i \equiv 1$ . For a cluster with multiple bumps, the crystal weight for each bump is calculated as

$$w_i = E_i \frac{\exp(-2.5r_i/r_M)}{\sum_j E_j \exp(-2.5r_j/r_M)}, \quad (8)$$

where the index  $j$  runs over all crystals in the cluster.  $r_M$  refers to the Molière radius, and  $r_i$  is the distance of the  $i$ th crystal from the centroid of the bump. At the outset, all weights are set to one. The process is then iterated, whereby the centroid position used in calculating  $r_i$  is determined from the weights of the previous iteration, until the bump centroid position is stable to within a tolerance of 1 mm.

The position of a bump is calculated using a center-of-gravity method with logarithmic, rather than linear weights [94,95],  $W_i = 4.0 +$

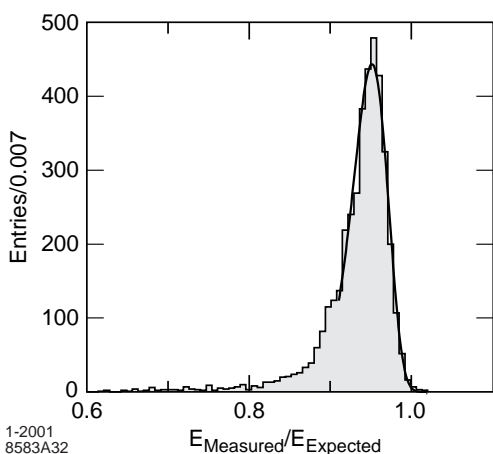


Figure 68. The ratio of the EMC measured energy to the expected energy for electrons from Bhabha scattering of 7.5 GeV/c. The solid line indicates a fit using a logarithmic function.

In  $E_i/E_{\text{bump}}$ , where only crystals with positive weights, *i.e.*,  $E_i > 0.0184 \times E_{\text{bump}}$ , are used in the calculation. This procedure emphasizes lower-energy crystals, while utilizing only those crystals that make up the core of the cluster. A systematic bias of the calculated polar angle originates from the non-projectivity of the crystals. This bias is corrected by a simple offset of  $-2.6$  mrad for  $\theta > 90^\circ$  and  $+2.6$  mrad for  $\theta < 90^\circ$ .

A bump is associated with a charged particle by projecting a track to the inner face of the calorimeter. The distance between the track impact point and the bump centroid is calculated, and if it is consistent with the angle and momentum of the track, the bump is associated with this charged particle. Otherwise, it is assumed to originate from a neutral particle.

On average, 15.8 clusters are detected per hadronic event, of which 10.2 are not associated with charged particle tracks. At current operating conditions, beam-induced background contributes on average 1.4 neutral clusters with energies above 20 MeV. This number is significantly smaller than the average number of crystals with energies above 10 MeV (see Section 3).

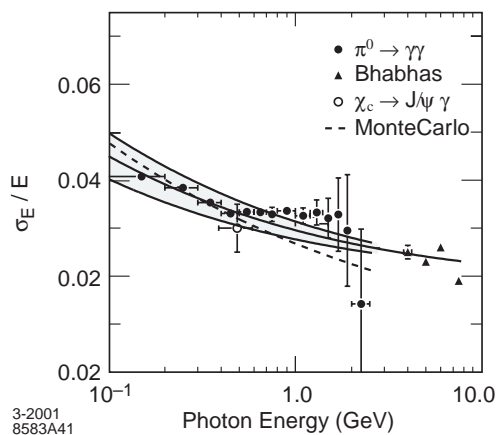


Figure 69. The energy resolution for the ECM measured for photons and electrons from various processes. The solid curve is a fit to Equation 6 and the shaded area denotes the rms error of the fit.

## 9.7. Performance

### 9.7.1. Energy Resolution

At low energy, the energy resolution of the EMC is measured directly with the radioactive source yielding  $\sigma_E/E = 5.0 \pm 0.8\%$  at 6.13 MeV (see Figure 66). At high energy, the resolution is derived from Bhabha scattering, where the energy of the detected shower can be predicted from the polar angle of the  $e^\pm$ . The measured resolution is  $\sigma_E/E = 1.9 \pm 0.07\%$  at 7.5 GeV (see Figure 68). Figure 69 shows the energy resolution extracted from a variety of processes as a function of energy. Below 2 GeV, the mass resolution of  $\pi^0$  and  $\eta$  mesons decaying into two photons of approximately equal energy is used to infer the EMC energy resolution [90]. The decay  $\chi_{c1} \rightarrow J/\psi \gamma$  provides a measurement at an average energy of about 500 MeV, and measurements at high energy are derived from Bhabha scattering. A fit to the energy dependence results in

$$\frac{\sigma_E}{E} = \frac{(2.32 \pm 0.30)\%}{\sqrt[4]{E(\text{GeV})}} \oplus (1.85 \pm 0.12)\%. \quad (9)$$

Values of these fitted parameters are higher than the somewhat optimistic design expectations, but they agree with detailed Monte Carlo simulations which include the contributions from electronic noise and beam background, as well as the impact

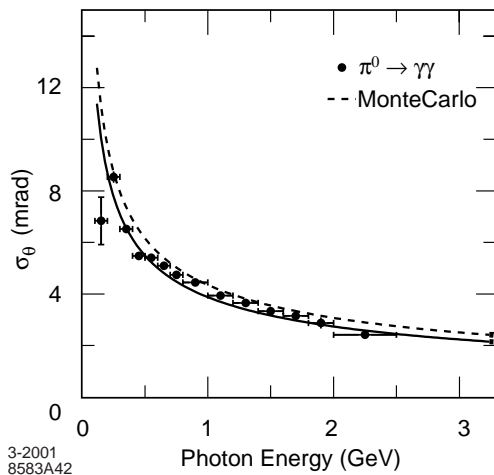


Figure 70. The angular resolution of the EMC for photons from  $\pi^0$  decays. The solid curve is a fit to Equation 7.

of the material and the energy thresholds.

### 9.7.2. Angular Resolution

The measurement of the angular resolution is based on the analysis of  $\pi^0$  and  $\eta$  decays to two photons of approximately equal energy. The result is presented in Figure 70. The resolution varies between about 12 mrad at low energies and 3 mrad at high energies. A fit to an empirical parameterization of the energy dependence results in

$$\begin{aligned} \sigma_\theta &= \sigma_\phi \\ &= \left( \frac{3.87 \pm 0.07}{\sqrt{E(\text{GeV})}} + 0.00 \pm 0.04 \right) \text{ mrad.} \end{aligned} \quad (10)$$

These fitted values are slightly better than would be expected from detailed Monte Carlo simulations.

### 9.7.3. $\pi^0$ Mass and Width

Figure 71 shows the two-photon invariant mass in  $B\bar{B}$  events. The reconstructed  $\pi^0$  mass is measured to be  $135.1 \text{ MeV}/c^2$  and is stable to better than 1% over the full photon energy range. The width of  $6.9 \text{ MeV}/c^2$  agrees well with the prediction obtained from detailed Monte-Carlo simulations. In low-occupancy  $\tau^+\tau^-$  events, the width is slightly smaller,  $6.5 \text{ MeV}/c^2$ , for  $\pi^0$  energies below 1 GeV. A similar improvement is also ob-

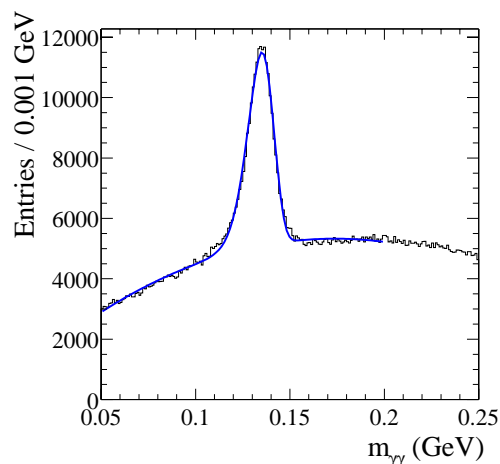


Figure 71. Invariant mass of two photons in  $B\bar{B}$  events. The energies of the photons and the  $\pi^0$  are required to exceed 30 MeV and 300 MeV, respectively. The solid line is a fit to the data.

served in analyses using selected isolated photons in hadronic events.

### 9.7.4. Electron Identification

Electrons are separated from charged hadrons primarily on the basis of the shower energy, lateral shower moments, and track momentum. In addition, the  $dE/dx$  energy loss in the DCH and the DIRC Cherenkov angle are required to be consistent with an electron. The most important variable for the discrimination of hadrons is the ratio of the shower energy to the track momentum ( $E/p$ ). Figure 72 shows the efficiency for electron identification and the pion misidentification probability as a function of momentum for two sets of selection criteria. The electron efficiency is measured using radiative Bhabhas and  $e^+e^- \rightarrow e^+e^-e^+e^-$  events. The pion misidentification probability is measured for selected charged pions from  $K_s^0$  decays and three-prong  $\tau$  decays. A tight (very tight) selector results in an efficiency plateau at 94.8% (88.1%) in the momentum range  $0.5 < p < 2 \text{ GeV}/c$ . The pion misidentification probability is of order 0.3% (0.15%) for the tight (very tight) selection criteria.

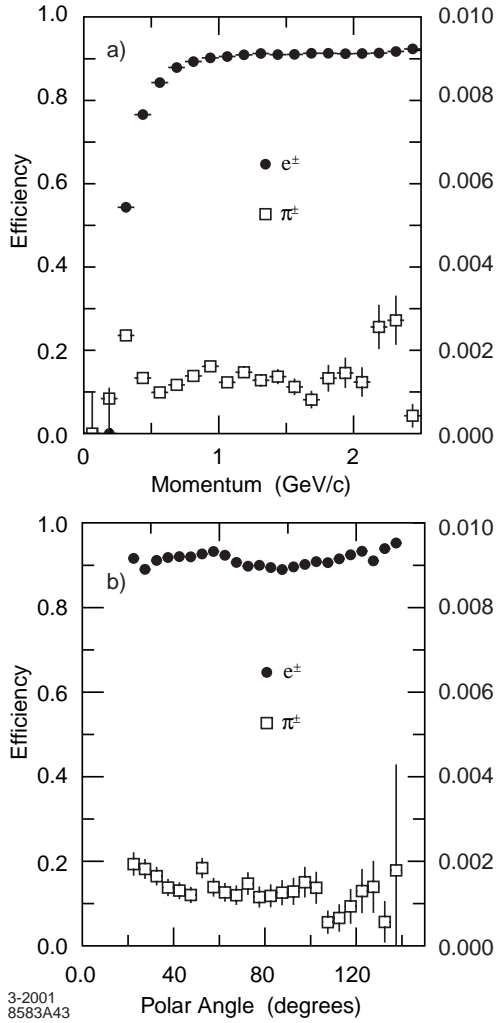


Figure 72. The electron efficiency and pion misidentification probability as a function of a) the particle momentum and b) the polar angle, measured in the laboratory system.

### 9.8. Summary

The EMC is presently performing close to design expectations. Improvements in the energy resolution are expected from the optimization of the feature-extraction algorithms designed to further reduce the electronics noise. Modifications to the electronics should allow for more precise calibrations. The expected noise reduction should permit a lower single-crystal readout threshold. However, this decrease in noise might be offset

by an increase in the beam background that is expected for higher luminosities and beam currents.